Detection and Analysis of Separated Flow Induced Vortical Structures

Stephen Snider,* Daniel Morse,* Guoning Chen,†
Sourabh V. Apte,‡ James A. Liburdy,§ and Eugene Zhang¶
Oregon State University, Corvallis, OR, 97331, USA

This study examines the ability to detect the dynamic interactions of vortical structures generated from a Helmholtz instability caused by separation over bluff bodies at large Reynolds number of approximately 10^4 based on a cross stream characteristic length of the geometry. Accordingly, two configurations, a square cylinder with normally incident flow and a thin airfoil with flow at an angle of attack of 20^0 are examined. Direct numerical simulation is used to obtain flow over the square cylinder. A time-resolved, three-component PIV data set is collected in a symmetry plane for the airfoil. Different approaches analyzing vector field and tensor field topologies are considered to identify vortical structures and local, swirl regions: (i) the Γ function that maps the degree of rotation rate (or pressure-gradients) to identify local swirl regions, (ii) Entity Connection Graph (ECG) that combines the Conley theory and Morse decomposition to identify vector field topology consisting of fixed points (sources, sinks, saddles, and periodic orbits), together with separatrices (links connecting them), and (iii) the λ_2 method that examines the gradient fields of velocity to identify local regions of pressure minima. Both velocity and pressure-gradient fields are analyzed for the DNS data, whereas only velocity field is used for the experimental data set. The vector-field topology requires spatial integration of the velocity or pressure-gradient fields. The tensor field topology, on the other hand, is based on gradients of the velocity of pressure-gradient vectors. A detailed comparison of these techniques is performed by applying them to velocity or pressure-based data and using spatial filtering of the data sets to identify the multiscale features of the flow. It is shown that various techniques provide useful information about the flowfield at different scales that can be used for further analysis of many fluid engineering problems of practical interest.

Nomenclature

Γ	Gamma Function
ECG	Entity Connection Graph
x	Variable value vector
u	Velocity, $\mathrm{m/s}$
ρ	Density, $\mathrm{kg/m^3}$
P	Pressure, $\mathrm{N/m^2}$
ν	Kinematic viscosity, $\mathrm{m^2/s}$
Subscript	
i	Variable number

I. Introduction

The ability to detect discrete flow structures in fluid flow environments is of growing interest to a wide variety of applications. For instance, large scale flow structures such as swirling, high shear rates regions and vortical structures

*Graduate Student, School of Mechanical, Industrial, and Manufacturing Engineering, 204 Rogers Hall, Corvallis, OR 97331, and AIAA Member.
†Graduate Student, School of Electrical Engineering and Computer Science, Corvallis, OR 97331.
‡Assistant Professor, School of Mechanical, Industrial, and Manufacturing Engineering, 204 Rogers Hall, Corvallis, OR 97331.
§Professor, School of Mechanical, Industrial, and Manufacturing Engineering, 204 Rogers Hall, Corvallis, OR 97331, and AIAA Member.
¶Assistant Professor, School of Electrical Engineering and Computer Science, Corvallis, OR 97331.

are thought to be controlling mechanisms for chaotic mixing, unsteady pressure fields that influence fluid-surface interactions, transport in multiphase flows, and a host of other applications. A robust means of developing an understanding of how these flow structures develop, evolve, decay, and interact is of fundamental importance. To achieve this goal there needs to be a quantitative measure of the relevant flow structures. This quantitative measure should also allow for spatial distinction among structures and a means of tracking such structures in the space and time domains. Since there may be many differing views on exactly what is a flow structure, there is a wide range of defining conditions for said structures. This results in a number of possible ways of detecting the desired flow structure. The unifying requirement of the detection schemes is that they provide a quantitative measure in a complex flow environment that defines the extent of the structure elements with an acceptable spatial and temporal resolution.

In this study the goal is to identify flow structures that are generated as a result of flow separation that occurs during flow over a bluff body. Such flow separation is indicative of a Kelvin-Helmhotz shearing instability[1–3] which results in a roll-up along a highly concentrated vortex sheet (or high shear region). Flows of this nature are extremely important in determining the dynamic loading on structures, in aerodynamic flight conditions, and drag forces on man-made vehicles or animals in motion. Presented are results for two such bodies, a square cross section object with separation at both the front and trailing edges and a thin airfoil at a high angle of attack (angle between the airfoil chord and flight direction is large causing leading edge flow separation). The flow patterns associated with both bodies are illustrated later in this paper, but the common element of concern for these flows is that the flow separation generates large swirling flow structures that are convected downstream as they change in size, shape and intensity.

II. Background

Traditionally, flow analysis involving turbulence and unsteady coherent structures that may be imbedded within the broad spectrum of turbulence has been based on collecting one-point and two-point statistics. However, there is a large and growing literature on swirl and vortical flow detection methods.[4–7] Proper Orthogonal Decomposition (POD),[6] the λ_2 (second eigenvalue) method,[4,8] and the Γ function,[7,9] among others, have been proposed and typically used for flow analysis. Specific identication of vortex structures (or pressure minima)[4,8,9] and correlating vortex shedding to leading edge separation,[3] have been applied. In addition to these, novel approaches developed in the scientific visualization community based on vector and tensor field visualization and topology extraction provide an alternative means to extract flow structure features.[10,11]

Recent advances in vector field topology focus on features such as fixed points, periodic orbits, and separatrices[12–16] in two-dimensions, which have been extended to three-dimensional steady state,[17–19] and time-dependent flows.[20–23] To address noise in the data sets, various flow simplification algorithms have been proposed that are either topology-based[14,16,24] or purely geometric.[25] Symmetric tensor field analysis has also been well investigated in two-dimensions.[26] The basic constituents of tensor topology, the wedges and trisectors have been identified in 2D, symmetric, second-order tensors. By tracking their evolution over time, these features can be combined to form more familiar field singularities such as saddles, nodes, centers, or foci.[26] This work has been extended to three-dimensions[27–29] and to time-varying tensor fields.[30] Tensor field simplification techniques have also been developed.[31,32] Analysis of asymmetric tensor fields such as the velocity gradient has been performed.[33,34] Zhang[34] performed topological analysis on the eigenvalues and eigenvectors of the velocity gradient to explore flow features such as regions of compression, dilation, rotation, and stretching.

In this work, the vector field topology extraction techniques is applied to flow data sets and compared with the traditional approaches based on the Γ and λ_2 methods. Furthermore, comparison of velocity-based and pressure-gradient based data and application of various feature extraction methods is performed to illustrate the potential of each technique when applied to different data sets. Two flow fields have been selected to explore the capabilities of flow structure detection during separation: (i) flow over a square cylinder, and (ii) flow over a flat thin airfoil at 20° angle of attack.

Flow over a square cylinder at $Re \approx 10,000$, based on the inlet velocity ($U_\infty = 1.5$ m/s), the cube size (L = 0.1 m and the fluid kinematic viscosity ($\nu = 15 \times 10^{-6}$ m^2/s), is obtained using direct numerical simulation. A three-dimensional simulation is performed with Dirichlet conditions at the inlet, a slip condition at the top and bottom surfaces, periodic conditions in the spanwise direction, and a convective boundary condition for the outlet. The direct numerical simulation is performed based on a colocated grid, fractional step algorithm[35–37] to collect the velocity and pressure data in space and time. The flow solver has been validated with available experimental data for a variety of flow configurations involving separated turbulent flows and swirling regions.[36–38]

The separated flow over an airfoil is obtained experimentally. Time-resolved PIV data of velocity components in a two dimensional plane along the centerline of a wing in a moderate Reynolds number ($Re = 6 \times 10^4$ based on the

chord length). The vector resolution of the PIV data is 0.684mm in a total field of field of 54 mm $\times$ 47 mm. The wing is at a 20^0 angle of attack (chord line relative to flow direction) and as such experiences a leading edge separation. The flow structures developing from this separation are of interest as they are convected downstream.

These two data sets were selected for a number of reasons. They both represent leading edge flow separation with significant vortical flow structure development. Both flows are at a reasonably high Reynolds number to assure a range of scales of motion and energy. Consequently, the robust nature of the vortex detection scheme can be evaluated for these multiscale flowfields. Also, there is a fundamental difference between experimentally and computationally obtained data sets. In general the computational simulation will contain both velocity and pressure field results over the full extent of the field of interest, while the experimental set will be limited to a velocity vector field (usually in two dimensions, and rarely more than two components). Consequently, experimental data sets lack the ability to use the pressure and/or the full dimensional field and its possible gradients as an indicator variable, or feature descriptor. As discussed below, several indicator variables are explored in this paper to assess the ability and distinctions of different variables to detect vortical flow structures.

The paper is arranged as follows. In the following section, the various flow analysis techniques are described in detail. These include both the vector field (velocity or pressure gradient) and tensor field (λ_2 method) analyses. These techniques are then applied to the square cylinder and airfoil data sets and compared to assess the similarities and differences of all detection schemes in identifying vortical flow features.

III. Flow Analysis Techniques

The flow descriptors used in this study are: (i) the Γ function, (ii) the Entity Connection Graphs (ECG[16]), and (iii) the λ_2 method. The Γ function and the ECG are based on a vector field such as velocity or pressure–gradient and require *integration* over a region surrounding the point of interest. The λ_2 method is based on the analysis of a tensor field (velocity gradient or pressure Hessian) and requires *differentiation* of a vector field at a point of interest.

A. The Γ-Function

A Γ function[9] has been proposed as a swirl strength parameter and used by one of the co-authors[7] to study pulsed jet in crossow. This method is based on a direct measure of the local swirl tendency of the flow field by calculating the vector orientation of the feature descriptor relative to a local radius vector at a given point within the flow field. Using the velocity vector $\overline{U}_M$ in the $\mathrm{x}-\mathrm{y}$ plane as the feature descriptor the swirl strength, Γ, is determined within a local grid area A_M by:

$$\Gamma(x,y) = \frac{1}{A_M}\int_{A_M} \frac{\left(\overline{PM}\times\overline{U}_M\right)\cdot\widehat{Z}dA}{\left(\|\overline{PM}\|\|\overline{U}_M\|\right)} \tag{1}$$

where $\widehat{Z}$ is a unit vector pointing out of the (x,y)-plane, and $\overline{PM}$ is the position vector of point M within the integration stencil and the point P. This is equivalent to the summation of the *sine* of the angle between the velocity vector at points within the area A_M and the position vector from these points to the position (x,y). Consequently, it is a measure of the local swirl strength filtered by the selection of the area A_M. Because of the local normalization, the swirl can be detected within regions of large dynamic range of velocity, which is advantageous in a separated flow region.

Note that the traditional definition of Γ function is based on the velocity vector. In order to define a similar feature detector based on the pressure-gradient vector, a new function denoted as Γ_p is defined as:

$$\Gamma_p(x,y) = \frac{1}{A_M}\int_{A_M} \frac{\left(\overline{PM}\times\overline{P}'_M\right)\cdot\widehat{Z}dA}{\left(\|\overline{PM}\|\|\overline{P}'_M\|\right)} \tag{2}$$

where $\overline{P}'_M = -(\nabla p)^{\perp}$ is the pressure gradient field rotated by 90^0 in the anti-clockwise direction. The pressure gradient normal to the radial vector centered at a given point within the flow is used, and is integrated about area A_M in a similar manner as shown above for the velocity vector. In this case the swirl indication is based on a local low pressure region which is scaled by the area averaged pressure gradient aligned towards a specific location within the flow. The area of integration is selected based on the spatial scale of interest.

B. Entity Connection Graphs (ECG)

Vector field topology in two-dimensions consists of fixed points (sources, sinks, saddles, and periodic orbits, Figure 1), together with separatrices (links connecting them). The fixed points identify specific flow features and the separatrices

provide possible paths and correlations between spatially varying structures. The fixed points and periodic orbits are the nodes in the ECG and separatrices are the edges. In addition, a periodic orbit can be connected directly to a source, sink, or another periodic orbit. These entities and their interconnection can be represented by a graph called *Entity Connection Graph* (*ECG*).[16] The ECGs of vector fields (for example, velocity and pressure gradient) can be used to identify specific flow features (such as vortex centers etc.)

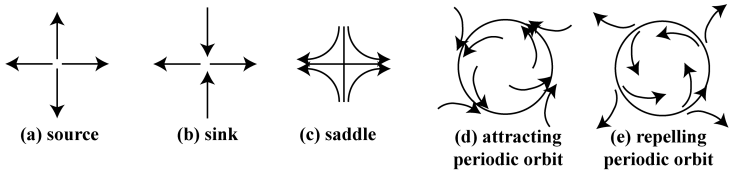

Figure 1. Schematic of vector field topology: (a) source, (b) sink, (c) saddle, (d) attracting and (e) repelling periodic orbits.

Mathematically, a vector field can be expressed in terms of a differential equation $\dot{x} = V(x)$. The set of solutions to it gives rise to a *flow* on the underlying domain M; that is a continuous function $\varphi : \mathbf{R} \times M \to M$ satisfying $\varphi(0,x) = x$, for all $x \in M$, and

$$\varphi(t, \varphi(s,x)) = \varphi(t+s,x) \tag{3}$$

for all $x \in M$ and $t,s \in \mathbf{R}$. Given $x \in M$, its *trajectory* is

$$\varphi(\mathbf{R},x) := \cup_{t\in\mathbf{R}} \varphi(t,x). \tag{4}$$

$S \subset M$ is an *invariant set* if $\varphi(t,S) = S$ for all $t \in \mathbf{R}$. Observe that for every $x \in M$, its trajectory is an invariant set. Other simple examples of invariant sets include the following. A point $x \in M$ is a *fixed point* if $\varphi(t,x) = x$ for all $t \in \mathbf{R}$. More generally, x is a *periodic point* if there exists $T > 0$ such that $\varphi(T,x) = x$. The trajectory of a periodic point is called a *periodic orbit*.

Consideration of the important qualitative structures associated with vector fields on a surface requires familiarity with hyperbolic fixed points, period orbits and separatrices. Let x_0 be a fixed point of a vector field $\dot{x} = V(x)$; that is $V(x_0) = 0$. The linearization of V about x_0, results in a 2×2 matrix $Df(x_0)$ which has two (potentially complex) eigenvalues $\sigma_1 + i\mu_1$ and $\sigma_2 + i\mu_2$. If $\sigma_1 \neq 0 \neq \sigma_2$, then x_0 is called a *hyperbolic fixed point*. Observe that on a surface there are three types of hyperbolic fixed points: *sinks* $\sigma_1, \sigma_2 < 0$, *saddles* $\sigma_1 < 0 < \sigma_2$, and *sources* $0 < \sigma_1, \sigma_2$. Systems with invariant sets such as periodic orbits are considered and the definition of the limit of a solution with respect to time is non-trivial. The *alpha* and *omega limit sets* of $x \in M$ are

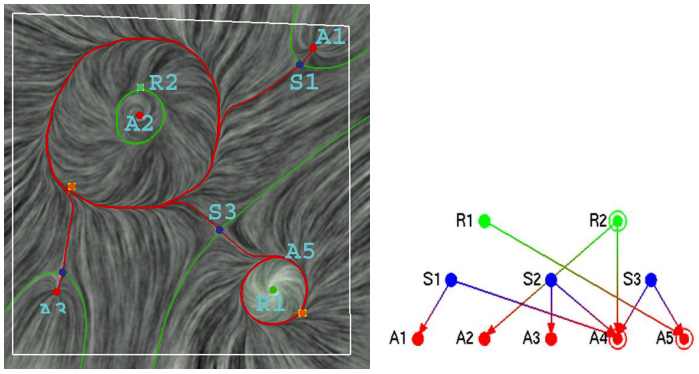

Figure 2. An example vector field (left) and its ECG[16] (right). The vector field contains a source (green), three sinks (red), three saddles (blue), a repelling periodic orbit (green), and two attracting periodic orbits (red). Separatrices that connect a saddle to a repeller (a source or a periodic orbit) are colored in green, and to an attractor (a sink or a periodic orbit) are colored in red. The fixed points and periodic orbits are the nodes in the ECG and separatrices are the edges.

$$\alpha(x) := \cap_{t<0} \mathrm{cl}(\varphi((-\infty,t),x)), \quad \omega(x) := \cap_{t>0} \mathrm{cl}(\varphi((t,\infty),x))$$

respectively. A periodic orbit $\mathcal{O}$ is *attracting* if there exists $\varepsilon > 0$ such that for every x which lies within a distance ε of $\mathcal{O}$, $\omega(x) = \mathcal{O}$. A *repelling* periodic orbit can be similarly defined ($\alpha(x) = \mathcal{O}$)). Finally, given a point $x_0 \in M$, its trajectory is a *separatrix* if the pair of limit sets $(\alpha(x), \omega(x))$ consist of a saddle fixed point and another object that can be a source, a sink, or a periodic orbit.

Figure 2 provides an example vector field (left). Fixed points are highlighted by colored dots (sources: green; sinks: red; saddles: blue). Periodic orbits are colored in green if repelling and in red if attracting. Separatrices that

terminate in a source or a repelling periodic orbit are shown in green and those terminate in a sink or an attracting periodic orbit are colored in red.

C. The λ_2 Method

The gradient of a vector field is an asymmetric tensor field, and the topological and geometric analysis of the vector gradient can provide additional insights to the understanding of the vector field itself. Here a well-known technique, the λ_2 method is applied to the experimental and numerical data sets. A newly developed descriptor based on the eigenvalue topology[34] has been developed in scientific visualization community and will be investigated in the future.

The local swirl within a flow can be determined based on a local pressure minimum by assessing the gradient fields of either velocity or pressure, this is designated as the λ_2 method. Jeong and Hussain[4] provide a thorough discussion of the various criteria and argue that the Hessian of pressure be used to identify local pressure minima, and hence the vortex core.

The equations of motion for an incompressible, Newtonian fluid with constant viscosity are given by the Navier Stokes equations:

$$\frac{\partial u_i}{\partial t} + \frac{\partial}{\partial x_j}(u_i u_j) = -\frac{1}{\rho}\frac{\partial P}{\partial x_i} + \nu \frac{\partial^2 u_i}{\partial x_j \partial x_j} \tag{5}$$

where u_i represents the components of the velocity vector, P the pressure field, and ν the kinematic viscosity. In addition, the velocity field must satisfy the divergence free constraint $u_{j,j} = 0$ for an incompressible fluid. Taking the gradient of the Navier-Stokes equation results in the relationship shown below between the pressure Hessian and the velocity gradient tensor separated into its symmetric and antisymmetric parts, S_{ij} and Ω_{ij}, respectively,

$$\underbrace{\left[\frac{D\mathrm{S}_{ij}}{Dt} + \mathrm{S}_{ik}\mathrm{S}_{kj} + \Omega_{ik}\Omega_{kj}\right]}_{\text{symmetric}} + \underbrace{\left[\frac{D\Omega_{ij}}{Dt} + \Omega_{ik}\mathrm{S}_{kj} + \mathrm{S}_{ik}\Omega_{kj}\right]}_{\text{antisymmetric}} = -\frac{1}{\rho}P_{,ij} + \nu u_{i,jkk}, \tag{6}$$

where $S_{ij} = (u_{i,j} + u_{j,i})/2$ and $\Omega_{ij} = (u_{i,j} - u_{j,i})/2$.

A direct meassure of the local pressure minimum can be obtained by evaluation of the eigenvalues of the pressure Hessian ($P_{,ij}$). Upon ordering the eigenvalues, a positive second eignevalue, denoted here as $\lambda_{2,p}$ expresses a local minimum. Alternatively, if the advective ($\frac{DS_{ij}}{Dt}$) and viscous terms ($\nu u_{i,jkk}$) of the above gradient equation are assumed small, the strain and rotation tensors, S_{ij} and Ω_{ij}, can be used to relate the effects of the local pressure minimum. Noting that the second bracket of the equation is identically zero (it is the well-known vorticity transport equation[4]), this method examines the eigenvalues of the remaining terms on the left hand side by using the velocity gradient fields and represents an estimation of the pressure Hessian ($P_{,ij}$). This is denoted as λ_2.

Majority of the works in turbulent, separated flow use the λ_2 method mainly because the velocity field can be directly measured in laboratories and hence its gradients can be obtained. However, detailed measurement of the pressure field in a region is usually not performed. In numerical simulations, both the velocity and pressure fields are computed and allows computation of different measures of swirl strengths. By examining the results using both the λ_2 and $\lambda_{2,p}$ it is possible to assess the detection sensitivities based on the velocity-based versus pressure-gradient based fields. In this case the exclusion of the covnective and viscous terms can be evaluated.

IV. Computation of Flow Descriptors

Computation of the vector field descriptors such as Γ & Γ_p and tensor field eigenvalues (λ_2 and $\lambda_{2,p}$) is fairly straightforward for both experimental and computational data sets. Once the velocity and pressure gradient fields are obtained these descriptors are extracted at each data-points and can be applied to multiple frames to evaluate the temporal evolution. In addition, the data-sets can be filtered using high and low-pass filters to extract the multiscale nature of the flow structures. Accordingly, any flow variable f can be written as $f = \tilde{f} + f'$, where $\tilde{f}$ and f' represent the low-pass and high-pass filtered data, respectively. A Gaussian filtering operation is used to obtain the low-pass data:

$$\tilde{f}(x,y) = \int_A (f \cdot G)\, dA; \quad G(x,y) = \frac{1}{2\pi\sigma^2}\exp\left(-\frac{x^2+y^2}{2\sigma^2}\right) \tag{7}$$

where σ represents the filter width. In this work, the filtered width used is *four* times the local grid resolution.

Evaluation of the vector field topology (ECG) needs description. The data sets provided by the experiments or simulation at particular grid nodes are first triangulated. The feature extraction domain is a triangular mesh in either a planar domain or a curved surface. The vector field is defined at the vertices only. To obtain values at a point on the edge or inside a triangle, a piecewise interpolation scheme is used. For planar domains, this is the well known piecewise linear interpolation scheme.[30] On surfaces, the scheme of Zhang et al.[24,32] that ensures vector field continuity in spite of the discontinuity in the surface normal is used.

Vector field topology for two-dimensional flows consists of fixed points, separatrices, and periodic orbits. An ECG is used to represent vector field topology.[16] To construct an ECG for a vector field represented on a triangular mesh, fixed points such as sources, sink, and saddles are first located and classified based on linearization inside each triangle. Next, periodic orbits are extracted by identifying regions of recurrence in the flow. In the third step, separatrices are computed by tracing streamlines from the saddles in their respective incoming and outgoing directions. This provides edges in the ECG that connect saddles to sources, sinks, and periodic orbits. Finally, edges in the ECG that directly connect between sources, sinks, and periodic orbits are determined by following the forward and reverse directions near periodic orbits that have not been reached by any separatrices.[16]

V. Results

The results of the flow detection schemes described previously were evaluated for the two data sets: (i) data in the symmetry plane from direct numerical simulation of the velocity and pressure fields for flow around a square cylinder, and (ii) experimentally obtained two dimensional velocity field around a thin wing at a fixed angle of attack. The experimental data is limited to velocity field and comparison of the vector (Γ and ECG) and tensor field topologies (λ_2 is performed. The DNS data set for flow over a square cylinder was evaluated using velocity-based and pressure-gradient based feature extraction techniques. This data set is used to compare the flow descriptors based on the velocity and pressure-gradient fields.

A. DNS Data on Flow Over a Square Cylinder

Figure 3 shows snapshots of velocity magnitude for flow over a square cylinder at $Re \approx 10,000$ obtained from direct numerical simulation. A three-dimensional simulation is performed with Dirichlet conditions at the inlet, a slip condition at the top and bottom surfaces, periodic conditions in the spanwise direction, and a convective boundary condition for the outlet. The edge of the square cylinder is 0.1 m, the inflow velocity is $U_\infty = 1.5$ m/s. A total of around 7–million Cartesian grid points are used in the computational domain. Also shown in Figure 3 are the three locations (near the leading edge and two near the edge of the boundary layer, $((-0.5, 0.079, 0)$ and $(-0.45, 0.079, 0))$ are marked at which temporal data is collected. Figures 3e–f show the pressure and velocity signals at these three locations. Figures 3g–h show the corresponding power spectra. Near the leading edge, the vortex shedding frequency is around 2 Hz. The corresponding Strouhal number $St = fL/U_\infty$ is 0.132. The flow separates at the leading edge corners and forms an oscillatory wake downstream giving rise to large scale vortical structures containing large levels of turbulent kinetic energy.

Figures 4 shows the flow analysis techniques applied to the cube data set. Specifically, the time evolution of Γ, Γ_p, λ_2, and ECG are plotted. The Γ, λ_2 and ECG are based on the velocity field, whereas the Γ_p is based on the pressure gradient. Note that the actual computations are full three-dimensional, however, only the two-dimensional data in the symmetry plane is analyzed. For the square cylinder, only the low-pass filtered data is shown. The goal of this analysis is to compare the various techniques for vortex detection.

Γ and Γ_p:

Figures 4a–b compare the Γ and Γ_p contours for the square cylinder. Both techniques identify the flow separation and swirling regions clearly. The flow separates at the corners of the leading edge. The top corner creates clockwise rotation whereas the bottom-one shows counter-clockwise rotation. The separated flow evolves over the cube surface and a strong wake region is visible downstream of the cylinder. Both techniques identify a strong, clockwise rotation in the wake of the cylinder. It is apparent that the pressure-gradient based Γ_p identifies more features than the velocity based Γ contours. This may be attributed to the fact that Γ_p is based on $(-\nabla P)$, and thus can capture the variations in flow velocity on a smaller scale (local grid size) compared to the velocity vector-based topology. Note that the Γ-function is obtained by performing spatial integration of the flow quantities (equation 1) at each grid location.

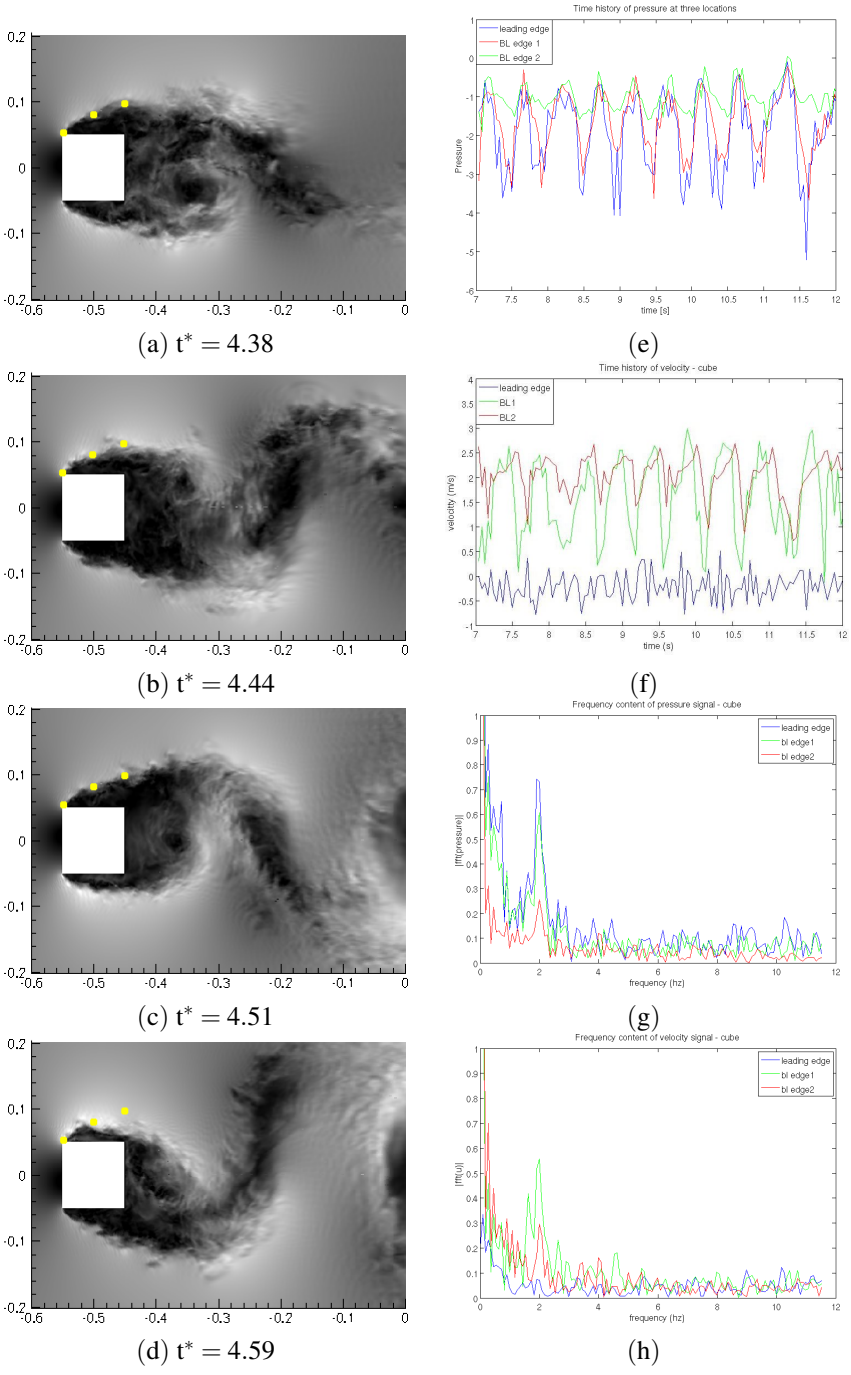

(a) $t^* = 4.38$ (e)

(b) $t^* = 4.44$ (f)

(c) $t^* = 4.51$ (g)

(d) $t^* = 4.59$ (h)

Figure 3. Direct numerical simulation of flow over a square cylinder at $Re = 10,000$. (a–d) the temporal evolution of velocity magnitude in the symmetry plane ($t^* = tU_\infty/L$), (e–f) pressure and velocity signal at three locations on the top surface, (g–h) the power spectra of pressure and velocity signals.

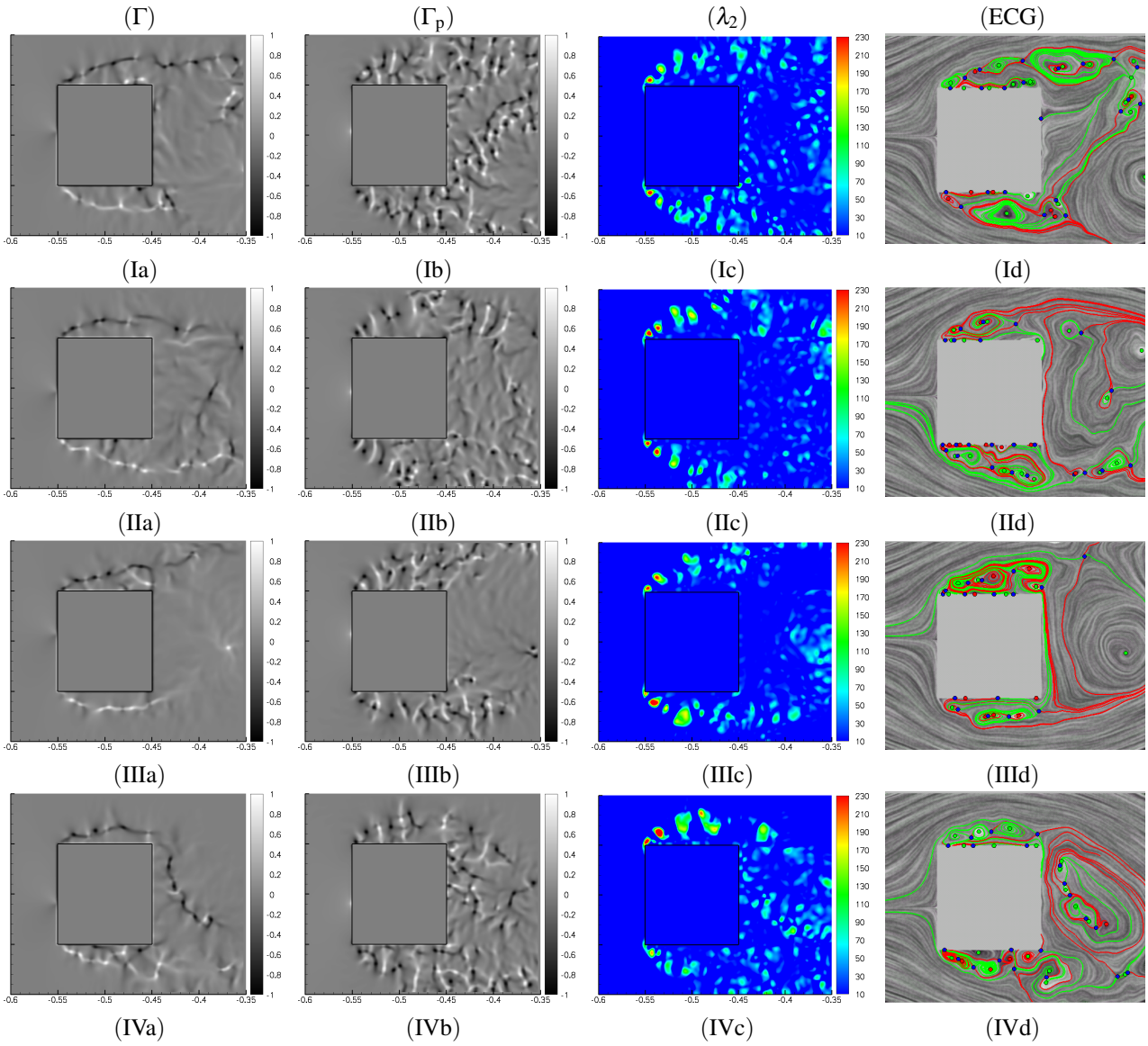

Figure 4. Vortex detection techniques applied to the velocity and pressure field of flow over a square cylinder. The time-evolution of Γ, Γ_p, λ_2, and ECG in the symmetry plane is plotted for $t^* = 4.38$,4.44,4.51, 4.59, respectively.

λ_2 and $\lambda_{2,p}$:

Figures 4c show the λ_2 contours obtained based on the velocity-gradient tensor. These tensor field topologies are based on the gradient of a vector field and identify *locally*, strong regions of swirl. Accordingly, strong swirl regions are obtained near the leading edge corners and also in the wake regions. The pressure Hessian based $\lambda_{2,p}$ shows similar regions of swirl (and is not shown). The contours are more spotty owing to the fact that the topology obtained is based on second derivatives of the pressure. The λ_2 contours try to find pressure minima based on the velocity-gradient based tensor. The temporal, convective, and viscous effects are assumed small to approximately locate the pressure minima. In the $\lambda_{2,p}$ approach, all effects are retained and consequently can locate the vortical regions more accurately.

ECG**:**

Figures 4d show the vector field topology as obtained from the velocity vector, respectively. Again, similar swirling patterns as observed by the Γ and Γ_p contours are visible. In this data-set sources (green), sinks (red), saddles (blue) and periodic orbits (attracting are red circles) are clearly visible. In addition, the separatrices connecting the fixed points are also shown. Again, the pressure-gradient based topology identifies more fixed points than the velocity field. However, the main vortical structures are identified by both. For example, the large circulation in the wake region (just behind the cylinder) is identified by green dots (source).

The separatrices show the link between the fixed points. It is observed that inside the separated flow region, the extent of the separatrices is large, indicating that the fixed points detected are correlated with distant flow events. This connectivity information is crucial for multiscale energy cascade mechanisms observed in many turbulent flows. By investigating the statistical nature of fixed points and their correlations, the path associated with energy transfer from large-scale to small scale flow structures can be identified. The ECG identifies circular paths around the vortical structures and the extent of the separatrices roughly scales with the size of the vortical structures. However, the strength of the vortex is not indicated by the ECG. The Γ function, on the other hand, provides information regarding the strength of the vortex.

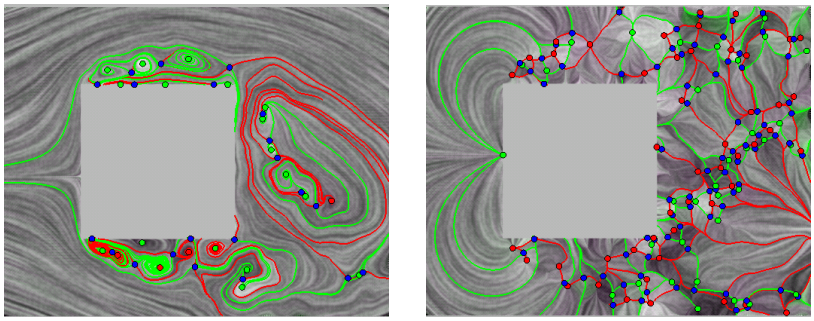

(a) Velocity based ECG (b) $-\nabla$P based ECG

Figure 5. Comparison of vector field topology obtained from velocity and pressure gradient vectors.

Figure 5 compares the velocity vector based and pressure-gradient based ECG for one frame. For the velocity-based ECG, the separatrices show circular paths spiraling around the source. The pressure-gradient based ECG, however, shows lines emanating from the source. This can be explained by considering a simple case of Rankine vortex (a combination of forced and free vortices):

$$v_\theta = \left\{ \omega r, \quad r \le a_c; \qquad \frac{\omega a_c^2}{r}, \quad r > a_c \right\},$$

where a_c is the radius of the core of the vortex, ω is the angular rotation associated with the vortex, r is the radial direction, and v_θ is the tangential velocity. The pressure gradient field inside the vortex core is simply given as $\partial p/\partial r = \rho\omega^2 r$. The pressure thus increases with increase in r and the gradient is truly radial. Thus, in a pure vortical flow, the pressure gradient lines are perpendicular to the velocity vector. The separatrices obtained from the pressure-gradient based ECG are seen to be approximately perpendicular to those obtained from the velocity-based ECG (see for example in the wake region). This is indicative of a strong vortical region. The extent of the separatrices roughly scales with the size of the vortical structure.

Figure 6 shows the power density spectra based on Γ, Γ_p, and λ_2 at three different locations near the top surface of the cube. The Γ_p and λ_2 spectra show distinct peaks for the middle data point (near the edge of the boundary layer). Note that the Γ_p is obtained from the gradient of the pressure, whereas the λ_2 is based on gradient of a velocity vector. These gradient based vector and tensor fields seem to detect the passing of vortical structures better than velocity based Γ function. The Γ function involves integration over a small region around the point of interest and may cause smearing of the spectral content of the vortical structures.

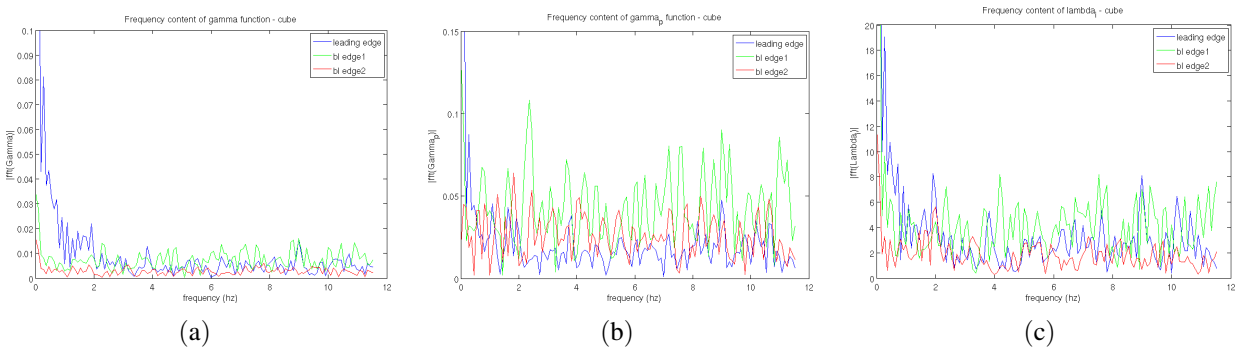

(a) (b) (c)

Figure 6. Power density spectra for flow over a square cylinder: Spectra are based on (a) Γ, (b) Γ_p, and (c) λ_2 at three near the top surface (as shown in Figure 3).

B. Airfoil Data

Figure 7 shows experimentally obtained velocity components in a two dimensional plane along the centerline of a wing in a moderate Reynolds number ($Re = 6 \times 10^4$ based on the chord length). This data set was obtained using particle image velocimetry and represents a snapshot of the velocity field with a vector resolution of 0.684mm in a total field of field of 54 mm $\times$ 47 mm. The wing is at a 20° angle of attack (chord line relative to flow direction) and as such experiences a leading edge separation. The flow structures developing from this separation are of interest as they are convected downstream. The energy spectrum associated with the leading edge region shows a broadband spectrum and is typical of these separated flows.

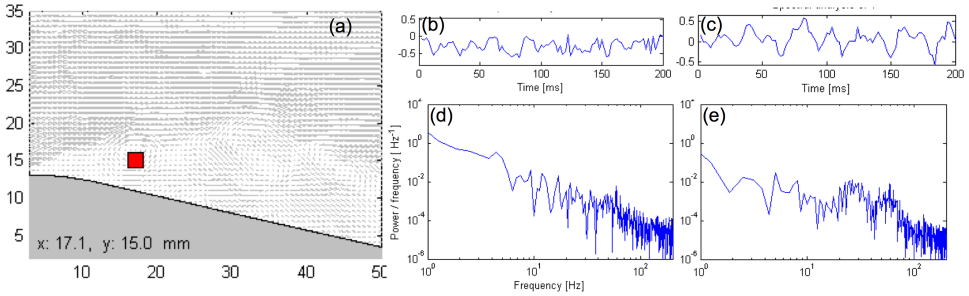

Figure 7. Time-resolved PIV data in the symmetry plane obtained at the OSU wind tunnel. (a) A close up view of the flow separation near the leading edge at 20^0 angle of attack, (b-c) time history of axial and vertical velocity signals, respectively, at x = 17.1 and y = 15 mm, (d-e) the corresponding power density spectra showing a broadband spectrum and time scales.

The wing flow field analysis is shown in Figure 8, where each row shows the flow features obtained from Γ, λ_2, and ECG, respectively. Each column represents the same feature extraction techniques applied to different time frames capturing the spatio-temporal evolution of the flow structures.

Γ Function:

The Γ function results (Figures 8a) illustrate the detection of well defined swirl that are separated into two main regions, the upper region is a clockwise (negative values) rotating stream that begins at the leading edge of the wing. This represents a flow instability that is generated by this localized separation which is then convected downstream. Below this region, very near the wing surface is a companion region of counterclockwise (positive values) rotating flow. Taken together these regions form a stream of clearly identified counter rotating vortices.

λ_2 Method:

Figures 8b show the tensor field topology as detected by the λ_2 method. As described in the previous section, the λ_2 method is associated with gradient of the vector-field (velocity in this case) and identifies local effects. Consequently, the original data set indicates clockwise rotating flow away from the airfoil surface, similar to the Γ-function. The

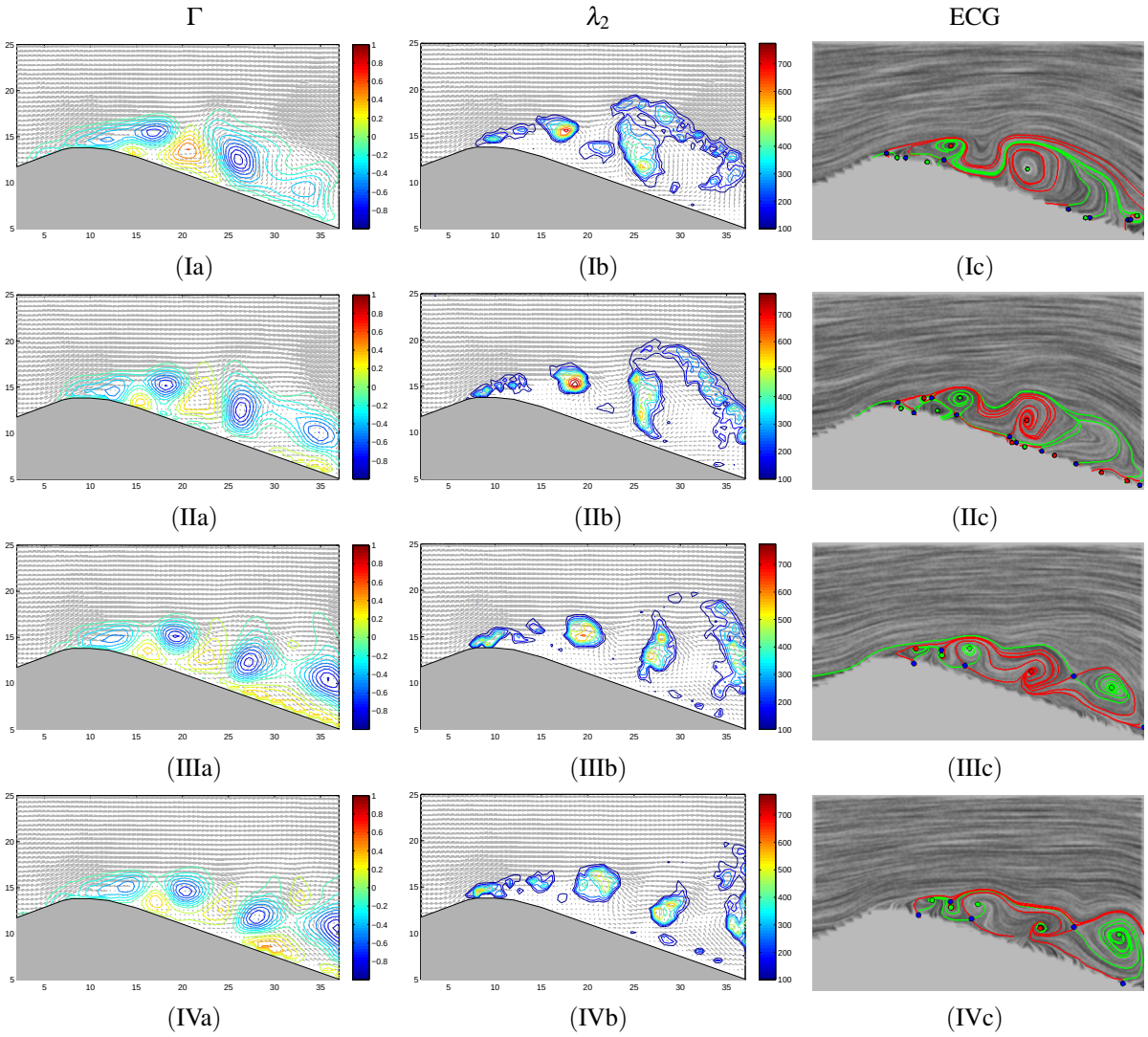

Figure 8. A comparison of various techniques for feature extraction applied to the experimental data set of flow over an airfoil with 20^0 angle of attack.

Γ-function is able to display well defined swirl flow pattern. While the λ_2 method does detect the strong clockwise rotating flow stream it only weakly detects the counterclockwise rotation near the surface.

ECG:

Figures 8c show the vector field topology (ECG). The ECG includes the instantaneous streamlines as a background texture in addition to the singularities (sources (green dots), sinks (red dots), and saddles (blue dots)), and the separatrices or the lines connecting the singularities (green line connects a saddle to a source or repeller, and red line connects the saddle to a sink or attractor). Repelling periodic orbits (green circles) are also clearly visible. The connectivity between the singularities indicate the spatial extent of the various flow events and their interactions. For example, in Figure 8c the two saddles (blue) near the leading edge show connection with the sources (green) on the downstream surface of the wing. This indicates how the flow patterns stretch and evolve through the flow and how surface effects are correlated to flow events far from the surface. Several fixed points inside and outside the separated flow region are visible. The separatrices show the link between the fixed points. It is observed that inside the separated flow region, the extent of the separatrices is large, indicating that the fixed points detected are correlated with distant flow events. However, outside the separated region (in the free-stream), the flow features are closely correlated by more local events. This vector-field based feature extraction technique shows similar vortical features as the Γ function. This connectivity information is crucial for multiscale energy cascade mechanisms observed in many turbulent flows.

VI. Conclusion

In this work, various techniques, based on vector and tensor fields, to identify multiscale features in turbulent, separated flows were analyzed in detail. Specifically, two techniques called (i) the Γ function, and (ii) ECG (the Entity Connection Graph) were used to deduce the vector field topology. In addition, the tensor field based on the velocity gradient or the pressure Hessian was analyzed by the λ_2 method. These flow feature extraction techniques were applied to two data sets: (i) direct numerical simulation based data of velocity and pressure-gradient fields for flow over a square cylinder, and (ii) experimental velocity field data of flow over a thin airfoil at 20° angle of attack. Both data sets were obtained at flow Reynolds number on the order of 10^4 based on the characteristic size of the bluff body. At these Reynolds numbers, the flow separates and large vortical structures are obtained that convect downstream. The various flow structure detection techniques were compared in detail.

The velocity and pressure-gradient fields were used to obtain the vector field topologies. The Γ function maps the degree of rotation rate (or pressure-gradient) to identify local swirl regions, and the ECG combines the Conley theory and Morse decomposition to identify vector field topology consisting of fixed points (sources, sinks, saddles, and periodic orbits), together with separatrices (links connecting them). For both data sets the two techniques detected similar flow features. The Γ function was able to provide the *strength* associated with the vortical structure. The ECG identified singularities in the flow and the separatrices showed the links between the singularities. The extent of the separatrix connecting two singularities was found to be roughly proportional to the *scale* of the vortex. It was observed that the λ_2 method for the tensor-field topology was capturing vortical structures on the small scale, whereas the extent of the vortices and large-scale features were observed in the vector field topology (Γ and ECG).

From the numerical simulations, the pressure-gradient based topology was obtained and indicated more flow features compared to the velocity-based analysis. The connectivity information between singularities or vortex centers as provided by the separatrices is an important feature that can be further used to analyze the multiscale energy cascade mechanisms observed in many turbulent flows.

These techniques can be further classified into global and local flow descriptors. The global descriptors are based on spatial integration of flow parameters (Γ, Γ_p and ECG) and thus extract large-scale features. The local techniques are based on the spatial derivatives of flow parameters (λ_2) and identify flow features on the scale of the grid size used to define the flowfield.

Acknowledgments

This work represents a collaborative effort at OSU between the experimental and computational analysis of fluid flow in Mechanical Engineering and scientific visualization in Computer Science. The work is partially support by NSF, AFOSR, and ONR. James Liburdy and Daniel Morse thank AFOSR for partial support under the grant FA-9550-05-0041. Sourabh Apte and Stephen Snider thank ONR and Dr. Ki-Han Kim for partial support under the grant N000140610697. Eugene Zhang and Guoning Chen thank NSF for the partial support under the NSF CAREER grant

CCF-0546881. Computations were performed on the San Diego Supercomputing Center's Datastar machine.

References

[1]Hoarau, Y. Braza, M., Ventikos, Y., Faghani, D., and Tzabiras, G., " Organized Modes and the Three Dimensional Transition to Turbulence in the Incompressible Flow Around a NACA0012 Wing," *J. Fluid Mech.*, Vol. 496, 2003, pp. 63–72.

[2]Nishimura H., and Taniike, Y., "Aerodynamic Characteristics of Fluctuating Forces on a Circular Cylinder," *J. Wind Eng. Ind. Aerodynamics*, Vol. 89, 2001, pp. 713–723.

[3]Sicot, C., Auburn, S., Loyer, S., and Devinant, P., "Unsteady Characteristics of the Static Stall of an Airfoil Subjected to Freestream Turbulence Level Up to 16%", *Exp. in Fluids*, Vol. 41, 2006, pp. 641–648.

[4]Jeong, J. and Hussain, F., "On the Identification of a Vortex," *J. Fluid Mech.*, Vol. 285, 1995, pp. 69–94.

[5]Burgmann, S. and Brucker, C. and Schroder, W., "Scanning PIV Measurements of a Laminar Separation Bubble," *Exp. Fluids*, Vol. 41, 2006, pp. 319–326.

[6]Weiland, C. and Vlachos, P., "Analysis of the Parallel Blade Vortex Interaction with Leading Edge Blowing Flow Control Using the Proper Orthogonal Decompositions," Proceedings FEDSM2007, Joint ASME/JSME Fluids Engineering Conf. July, San Diego, 2007.

[7]Dano, B and Liburdy, J., "Vortical Structures of a 45^0 Inclined Pulsed Jet in Crossflow," AIAA 2006-3542, Fluid Dynamics Conf., San Francisco, CA, 2006.

[8]Adrian, R., Christiansen, K., and Liu, Z., "Analysis and Interpretation of Instantaneous Velocity Fields," *Exp. Fluids*, Vol. 41, 2000, pp. 319–326.

[9]Graftieaux, L., Michard, M., and Grosjean, N., "Combining PIV, POD and Vortex Identification Algorithms for the Study of Unsteady Turbulent Swirling Flows," *Meas. Sci. Tech.*, Vol. 12, 2001, pp. 1422–1429.

[10]Laramee, R.S., Hauser, H., Doleisch, H., Post, F.H., Vrolijk, B., and Weiskopf, D., "The State of the Art in Flow Visualization: Dense and Texture-Based Techniques," *Computer Graphics Forum*, Vol. 23, No. 2, 2004, pp. 203–221.

[11]Laramee, R.S., Hauser, H., Zhao, L., Post, F.H., "Topology Based Flow Visualization: The State of the Art," *The Topology-Based Methods in Visualization Workshop* (TopoInVis 2005), 2006.

[12]Helman, J.L., and Hesselink, L., "Visualizing Vector Field Topology in Fluid Flows," *IEEE Computer Graphics and Applications*, Vol. 11, No. 3, 1991, pp. 36–46.

[13]Scheuermann, G., Krüger, H., Menzel, M., and Rockwood, A.P., "Visualizing Nonlinear Vector Field Topology," *IEEE Transactions on Visualization and Computer Graphics*, Vol. 4, No. 2, 1998, pp. 109–116.

[14]Tricoche, X. and Scheuermann, G., "Continuous Topology Simplification of Planar Vector Fields," *Proceedings IEEE Visualization*, 2001, pp. 159–166.

[15]Polthier, K., and Preuß, E., "Identifying Vector Fields Singularities using a Discrete Hodge Decomposition", *Mathematical Visualization III, Ed: H.C. Hege, K. Polthier*, Springer Verlag, 2003, pp 112-134.

[16]Chen,G., Mischaikow, K., Laramee, R.S., Pilarczyk, P., and Zhang, E., "Vector Field Editing and Periodic Orbit Extraction Using Morse Decomposition," *IEEE Transactions on Visualization and Computer Graphics*, Vol. 13, No. 4, 2007, pp. 769–785.

[17]Globus, A., Levit, C., and Lasinski, T., "A Tool for Visualizing the Topology of Three-Dimensional Vector Fields," *Proceedings IEEE Visualization*, 1991, pp. 33–40.

[18]Theisel, H., Weinkauf, T., Hege, H.-C., and Seidel, H.-P, "Saddle Connectors–An Approach to Visualizing the Topological Skeleton of Complex 3D Vector Fields," *Proceedings IEEE Visualization* 2003, pp. 225–232.

[19]Mahrous, K., Bennett, J.C., Scheuermann, G., Hamann, B., and Joy, K.I. "Topological Segmentation in Three-Dimensional Vector Felds," *IEEE Transactions on Visualization and Computer Graphics*, Vol. 10, No. 2, 2004, pp. 198–205.

[20]Tricoche, X., Wischgoll, T., Scheuermann, G., and Hagen, H., "Topology Tracking for the Visualization of Time-Dependent Two-Dimensional Flows," *Computers & Graphics*, Vol. 26, No. 2, 2002, pp. 249–257.

[21]Theisel, H., and Seidel, H.-P., "Feature Flow Fields," *Proceedings of the Joint Eurographics - IEEE TCVG Symposium on Visualization (VisSym 03)*, 2003, pp. 141–148.

[22]Theisel, H., Weinkauf, T., Hege, H.-C., and Seidel, H.-P., "Stream Line and Path Line Oriented Topology for 2D Time-Dependent Vector Fields," *Proceedings IEEE Visualization* 2004, pp. 321–328.

[23]Garth, C., Tricoche, X., and Scheuermann, G., "Tracking of Vector Field Singularities in Unstructured 3D Time-Dependent Datasets," *Proceedings IEEE Visualization* 2004, pp. 329–335.

[24]E. Zhang, K. Mischaikow, and G. Turk, Vector Field Design on Surfaces, ACM Transactions on Graphics, vol. 25, no. 4, pp. 1294–1326, 2006.

[25]Y. Tong, S. Lombeyda, A. Hirani, and M. Desbrun, Discrete Multiscale Vector Field Decomposition, ACM Transactions on Graphics (SIGGRAPH 2003), vol. 22, no. 3, pp. 445–452, 2003.

[26]Delmarcelle, T. and Hesselink, L., "The Topology of Symmetric, Second-Order Tensor Fields," *Proceedings IEEE Visualization*, 1994.

[27]Hesselink, L., Levy, Y., and Lavin, Y., "The Topology of Symmetric, Second-Order 3D Tensor Fields," *IEEE Transactions on Visualization and Computer Graphics*, Vol. 3, No. 1, 1997, pp. 1–11.

[28]Zheng, X., and Pang, A., "Topological Lines in 3D Tensor Fields," *Proceedings IEEE Visualization*, 2004, pp. 313–320.

[29]Zheng, X., Parlett B., and Pang, A., "Topological Structures of 3D Tensor Fields," *Proceedings IEEE Visualization*, 2005, pp. 551–558.

[30]Tricoche, X., Scheuermann, G., and Hagen, H., "Tensor Topology Tracking: a Visualization Method for Time-Dependent 2D Symmetric Tensor Fields," *Computer Graphics Forum (Eurographics 2001)*, Vol. 20, No. 3 2001, pp. 461–470.

[31]Tricoche, X., Scheuermann, G., and Hagen, H., *Topology Simplification of Symmetric, Second-Order 2D Tensor Fields*, Hierarchical and Geometrical Methods, Springer, 2003.

[32]Zhang, E., Hays, J., and Turk, G., "Interactive Tensor Field Design and Visualization on Surfaces," *IEEE Transactions on Visualization and Computer Graphics*, Vol. 13, No. 1, 2007, pp. 94–107.

[33]Zheng, X., and Pang, A., "2D Asymmetric Tensor Analysis," *IEEE Proceedings on Visualization*, 2005, pp. 3–10.

[34]Zhang, E., Yeh, H., Lin, Z., and Laramee, R., "Topological Analysis of Asymmetric Tensor Fields for Flow Visualization," Oregon State University, Tech. Rep. CS07-50-01, 2007, Online available: http://eecs.oregonstate.edu/library/files/2007-39/asymtenfld.pdf.

[35]Mahesh, K., Constantinescu, G., and Moin, P., "A New Time-Accurate Finite-Volume Fractional-Step Algorithm for Prediction of Turbulent Flows on Unstructured Hybrid Meshes," *J. Comp. Phy.*, Vol. 197, 2004, pp. 215–240.

[36]Mahesh, K., Constantinescu, G., Apte, S,V, Iaccarino, G., Ham, F., and Moin, P., "Large-Eddy Simulation of Reacting Turbulent Flows in Complex Geometries," *ASME J. App. Mech.*, Vol. 438, 2006, pp. 101–128.

[37]Moin, P., and Apte, S.V., "Large Eddy Simulation of Multiphase Reacting Flows in Complex Combustors," *AIAA J. (special issue on 'Combustion Modeling and LES: Development and Validation Needs for Gas Turbine Combustors)*, Vol. 44, 2006, pp. 698–710.

[38]APTE, S. V., MAHESH, K., MOIN, P., & OEFELEIN, J.C., 2003a, Large-Eddy Simulation of Swirling Particle-Laden Flows in a Coaxial-Jet Combustor. *Int. J. Mult. Flow* **29**, 1311-1331.